Article

A thermotropic liquid crystal enables efficient and stable perovskite solar modules

Yi Yang [1,8], Cheng Liu [1,8], Yong Ding [2,3,8], Bin Ding [2,8], Jian Xu [4,8], Ao Liu [1], Jiaqi Yu [1], Luke Grater [4], Huihui Zhu[1], Shreyash Sudhakar Hadke[5], Vinod K. Sangwan [5], Abdulaziz S. R. Bati [1], Xiaobing Hu [5], Jiantao Li [6], So Min Park [1], Mark C. Hersam [1,5,7], Bin Chen [1]✉, Mohammad Khaja Nazeeruddin [2]✉, Mercouri G. Kanatzidis [1]✉ & Edward H. Sargent [1,4,7]✉

Perovskite solar cells have seen impressive progress in performance and stability, yet maintaining efficiency while scaling area remains a challenge. Here we find that additives commonly used to passivate large-area perovskite films often co-precipitate during perovskite crystallization and aggregate at interfaces, contributing to defects and to spatial inhomogeneity. We develop design criteria for additives to prevent their evaporative precipitation and enable uniform passivation of defects. We explored liquid crystals with melting point below the perovskite processing temperature, functionalization for defect passivation and hydrophobicity to improve device stability. We find that thermotropic liquid crystals such as 3,4,5-trifluoro-4′-(*trans*-4-propylcyclohexyl)biphenyl enable large-area perovskite films that are uniform, low in defects and stable against environmental stress factors. We demonstrate modules with a certified stabilized efficiency of 21.1% at an aperture area of 31 cm^2 and enhanced stability under damp-heat conditions (ISOS-D-3, 85% relative humidity, 85 °C) with T_{86} (the duration for the efficiency to decay to 86% of the initial value) of 1,200 h, and reverse bias with (ISOS-V-1, negative maximum-power-point voltage) and without bypass diodes.

Perovskite solar cells (PSCs) have seen impressive progress[1–4], including in methods of manufacture such as slot-die coating and vacuum quenching. Nevertheless, a gap exists in module efficiency compared with cell efficiency: the highest certified stabilized efficiency of perovskite modules exceeding 30 cm^2 has been so far limited to 19.5% (refs. 5–7). Defects are known to play a significant role in this, being attributed to local perturbations in stoichiometry[8,9].

Incorporating additives such as Lewis acids and bases into the precursor solution has been seen to suppress defect formation[10–13]. However, these additives tend to aggregate in the perovskite film during co-precipitation with perovskite, a process that occurs while the solvent evaporates[14–16]. This aggregation contributes to inhomogeneity within the perovskite film, a challenging problem for scale[17]. This motivated us to contemplate additives capable of preventing

[1]Department of Chemistry, Northwestern University, Evanston, IL, USA. [2]Institute of Chemical Sciences and Engineering, EPFL, Lausanne, Switzerland. [3]State Key Laboratory of Alternate Electrical Power System with Renewable Energy Sources, North China Electric Power University, Beijing, China. [4]Department of Electrical and Computer Engineering, University of Toronto, Toronto, Ontario, Canada. [5]Department of Materials Science and Engineering, Northwestern University, Evanston, IL, USA. [6]Chemical Sciences and Engineering Division, Argonne National Laboratory, Lemont, IL, USA. [7]Department of Electrical and Computer Engineering, Northwestern University, Evanston, IL, USA. [8]These authors contributed equally: Yi Yang, Cheng Liu, Yong Ding, Bin Ding, Jian Xu. ✉e-mail: bin.chen@northwestern.edu; mdkhaja.nazeeruddin@epfl.ch; m-kanatzidis@northwestern.edu; ted.sargent@northwestern.edu
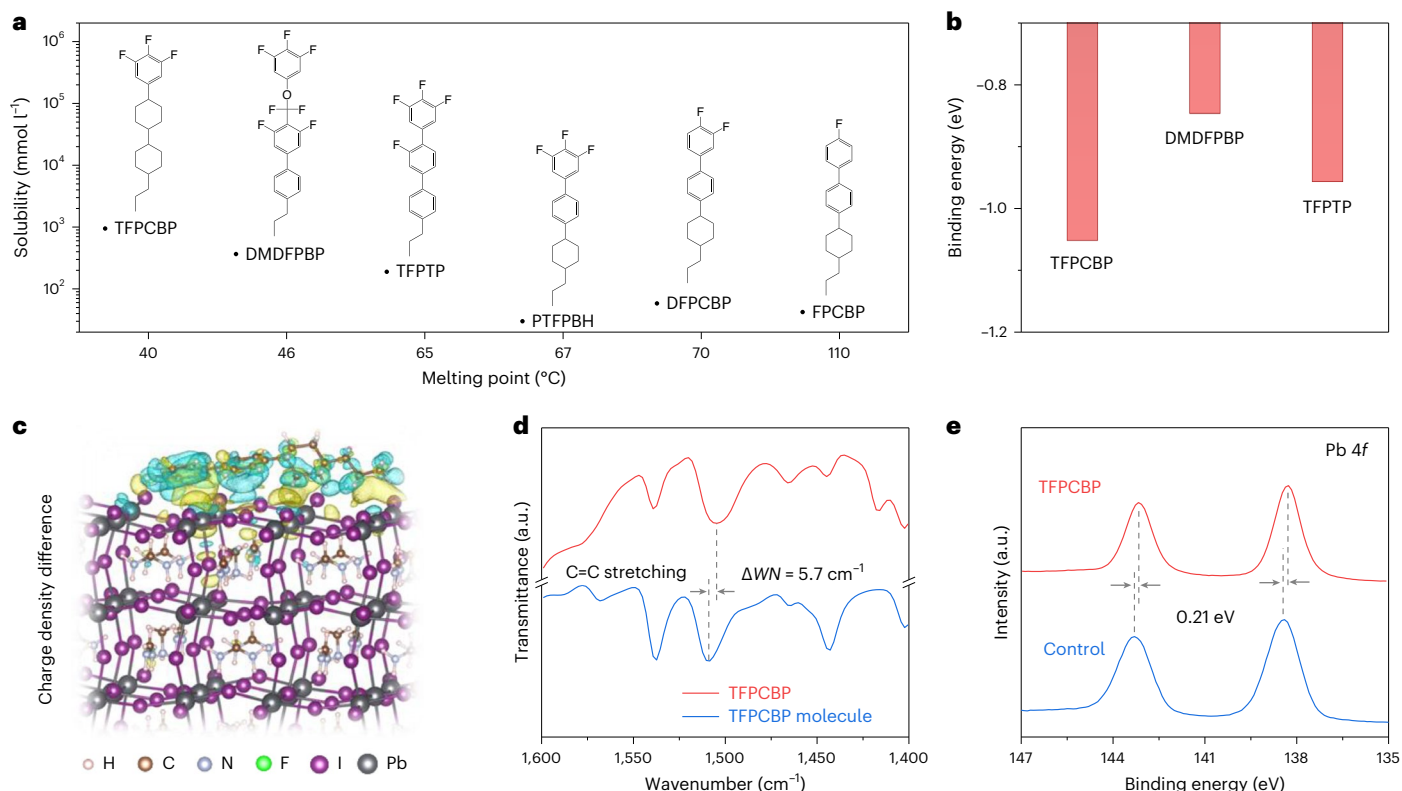
Fig. 1 | Characterization of liquid crystals and interactions with perovskite. **a**, A comparison of the solubility in *N,N*-dimethylformamide and the melting point of liquid crystal molecules, including 4-fluoro-4′-(*trans*-4-propylcyclohexyl)biphenyl (FPCBP), 3,4-difluoro-4′-(*trans*-4-propylcyclohexyl)biphenyl (DFPCBP), 3,4,5-trifluoro-4′-(*trans*-4-propylcyclohexyl)biphenyl (TFPCBP), *trans,trans*-4′-propyl-4-(3,4,5-trifluorophenyl)bicyclohexyl (PTFPBH), 2′,3,4,5-tetrafluoro-4″-propyl-1,1′:4′,1″-terphenyl (TFPTP) and 4-[difluoro(3,4,5-trifluorophenoxy)methyl]-3,5-difluoro-4′-propylbiphenyl (DMDFPBP). **b**, The binding energy of the −$C_6H_2F_3$ group attached to the iodine vacancy defect. **c**, The charge density difference (blue, depletion; yellow, accumulation) of TFPCBP anchoring on the Pb–I terminated perovskite surface. **d**, FTIR spectra of the TFPCBP-embedded perovskite film and the TFPCBP powder. The carbon–carbon stretching vibration peaks are located at wavenumbers (WNs) of 1,503.8 and 1,509.5 cm^{-1} for the TFPCBP-embedded perovskite and TFPCBP molecule, respectively, with the frequency shift calculated from their difference. **e**, XPS spectra of Pb 4*f* core levels. Dashed lines indicate the positions of the Pb 4*f* XPS peaks for each sample, with the binding energy shift calculated from their difference.

evaporative precipitation and crystallization to reduce both defects and insulating inclusions.

In this Article, we describe an exploration of the use of thermotropic liquid crystals to enhance the diffusion of additives during perovskite crystallization. We find that the approach increases homogeneity in the spatial distribution of additives. We find that the even distribution of liquid crystal molecules better passivates iodine vacancy defects and reduces non-radiative recombination as well as facilitating more uniform perovskite films over large areas. Liquid crystal-incorporating PSCs achieve a power conversion efficiency (PCE) of 25.6%, and liquid crystal-based perovskite modules with an aperture area of 31 cm^2 achieve a certified efficiency of 21.6% (stabilized 21.1%) along with documented operating and reverse bias stability.

## Liquid crystal properties and interactions with perovskite
We screened a family of six liquid crystals (Supplementary Text, Supplementary Table 1 and Supplementary Figs. 1 and 2), seeking to look across a range of melting points, solubilities and binding energies with regard to defect sites on perovskite (Fig. 1a,b). We noted one candidate, that is, 3,4,5-trifluoro-4′-(*trans*-4-propylcyclohexyl)biphenyl (TFPCBP), that showed particular promise with respect to photoluminescence (PL) map uniformity (Supplementary Fig. 3) and device performance (Supplementary Fig. 4).

We carried out density functional theory (DFT) calculations to study the interaction between TFPCBP and the perovskite. The neutral TFPCBP molecule has a dipole moment of 4.15 Debye (Supplementary Fig. 5) owing to the electron-withdrawing nature of the phenyl and F functional groups. We found that, when this molecule interacts with formamidinium–I and Pb–I terminated perovskite surfaces, TFPCBP exhibits a charge redistribution, particularly on the side (−$C_6H_2F_3$) characterized by the lowest electrostatic potential (Fig. 1c and Supplementary Fig. 6). Experimental analysis using Fourier-transform infra-red (FTIR) spectroscopy showed a frequency shift of 5 cm^{-1} at approximately 1500 cm^{-1} (Fig. 1d), corresponding to the carbon–carbon stretching vibrations in the aromatic ring[18], and a shift of approximately 2 cm^{-1} at 1,040 cm^{-1}, related to the carbon–fluorine stretching vibrations (Supplementary Fig. 7)[19]. High-resolution X-ray photoelectron spectroscopy (XPS) analysis provided additional evidence of molecular interactions between TFPCBP and perovskite. The core level spectra of Pb 4*f* in the perovskite exhibited a shift towards lower binding energy, and of F 1*s* in TFPCBP to higher binding energy, when TFPCBP was incorporated into the perovskite film (Fig. 1e and Supplementary Fig. 8).

Homogeneity and optoelectronic properties
Scanning electron microscopy (SEM) images (Fig. 2a) showed that the perovskite film with TFPCBP had crystal grains of approximately two times the linear dimensions of controls, attributed to the slower crystal growth as observed from in situ microscopy images (Supplementary Fig. 9). This was consistent with the enhanced crystallinity and a tightened full-width at half-maximum (FWHM) seen in X-ray diffraction analysis (Fig. 2b). The crystal orientation was not affected by
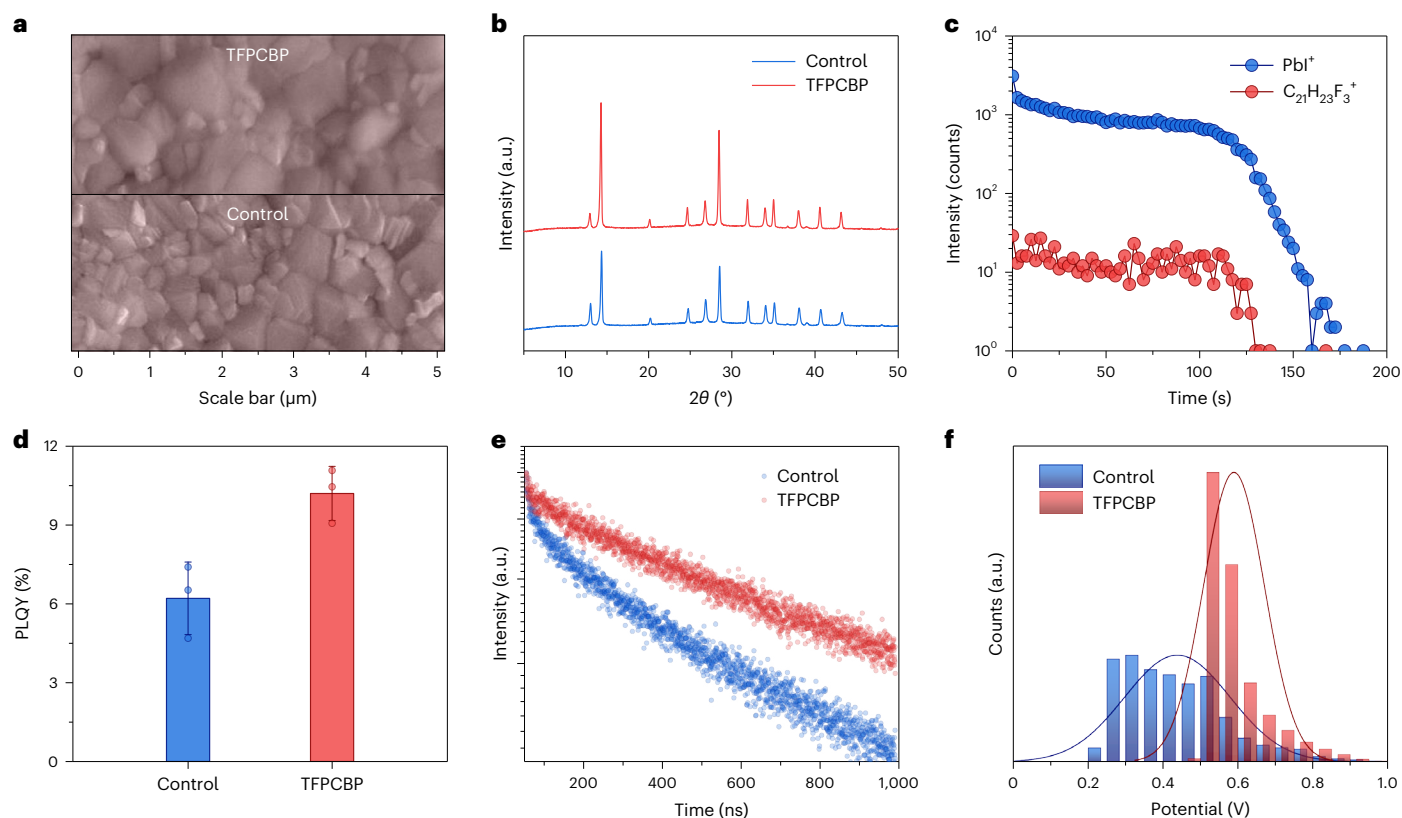
Fig. 2 | Characterization of perovskite films. a, SEM images of control and TFPCBP perovskite films. **b**, X-ray diffraction patterns of the perovskite films. **c**, SIMS depth profile of $C_{21}H_{23}F_3^+$ for the perovskite film with TFPCBP. **d**, PLQY of the fabricated perovskite films. Data presented as mean ± s.d. of three films measured for each condition. **e**, TRPL spectra of perovskite films on glass substrates. **f**, KPFM potential distribution of perovskite films over a $5 \times 5 \ \mu m^2$ region. In each condition, 65,536 data points were collected and analysed. Solid lines represent the statistical distribution curve fitted using a Gaussian distribution model.

TFPCBP as shown in grazing-incidence wide-angle X-ray scattering (GIWAXS) imaging (Supplementary Fig. 10). The control film showed the diffraction of δ-phase FAPbI$_3$ at the scattering vector in the specular direction ($\mathbf{q}_z$) of 0.88 Å^{-1}, which was caused by perovskite degradation during ex situ measurement with exposure to humid air. In contrast, the TFPCPB film lacked evidence of a δ phase, which we assign to the hydrophobicity of TFPCBP (Supplementary Fig. 11). Time-of-flight secondary ion mass spectrometry (ToF-SIMS) showed that the TFPCBP molecule was uniformly distributed throughout the film, that is, it did not accumulate at the interface/surface (Fig. 2c).

Transmission electron microscopy (TEM) revealed the distribution of TFPCBP at grain boundaries and the absence of ordered structure (Supplementary Fig. 12). This agrees with the absence of the TFPCBP peak in the X-ray diffraction pattern of TFPCBP perovskite films (Fig. 2b and Supplementary Fig. 13). This could be attributed to: (1) the low melting point of TFPCBP, which is expected to facilitate strong molecular diffusion during perovskite crystallization, resulting in a uniform distribution along the narrow grain boundaries (Supplementary Fig. 14), and (2) the relatively large TFPCBP molecules, which hinder aggregation/crystallization of TFPCBP due to spatial confinement. We link this uniform distribution of additives without aggregation to evidence of more uniform passivation, as witnessed using PL mapping and potential mapping described below.

Also, using DFT, we looked at how TFPCBP could potentially affect the defect formation in perovskite films by considering the most common, iodine vacancy defect[20]. Calculations were based on the perovskite surface vacancy, while the surface here refers to any grain surfaces, including grain boundaries and the film surface, consistent with the TFPCBP distribution observed by TEM and ToF-SIMS. We simulated two adsorption modes of TFPCBP (Supplementary Fig. 15) and found

that the binding energy of the $-C_6H_2F_3$ group attached to the defect site (−1.05 eV) was higher than that of the alkyl chain group attached to the defect site (−0.47 eV), pointing to $-C_6H_2F_3$ as the most active functional group in TFPCBP from the point of view of the interaction with the perovskite surface. Notably, the introduction of TFPCBP led to an increase in the iodine vacancy formation energy from 1.18 to 1.27 eV, indicating its capacity to suppress defects. Consistent with this, the average photoluminescence quantum yield (PLQY) of the perovskite film was increased, as was the excited state lifetime (890 versus 520 ns) following incorporation of TFPCBP (Fig. 2d,e). Additionally, a decreased trap density of states was observed in space charge-limited current studies (Supplementary Fig. 16).

PL maps show that TFPCBP films have enhanced PL emission and a narrower emission distribution (Supplementary Fig. 17), indicating improved film homogeneity and suppressed defect sites. Unintended defects can cause strong potential fluctuations, as shown in the Kelvin probe force microscopy (KPFM) potential distribution (Fig. 2f). The contact potential difference (CPD) is a critical parameter in the performance of electronic devices, especially thin film devices, because it affects the energy level alignment at the interface and, hence, the efficiency of charge transfer and transport across the interface[21]. The CPD can also influence the optical properties of thin films by altering the bandgap of the materials at the interface, thereby affecting the absorption and emission of light. Introducing TFPCBP led to a lower r.m.s. deviation of CPD, reduced from approximately 100 to 80 mV.

Photovoltaic performance
We fabricated solar cells in an n–i–p configuration, employing a fluorine-doped tin oxide (FTO)/SnO$_2$/perovskite/2,2′,7,7′-tetrakis (N,N-di-p-methoxyphenylamine)-9,9′-spirobifluorene (spiro-OMeTAD)/
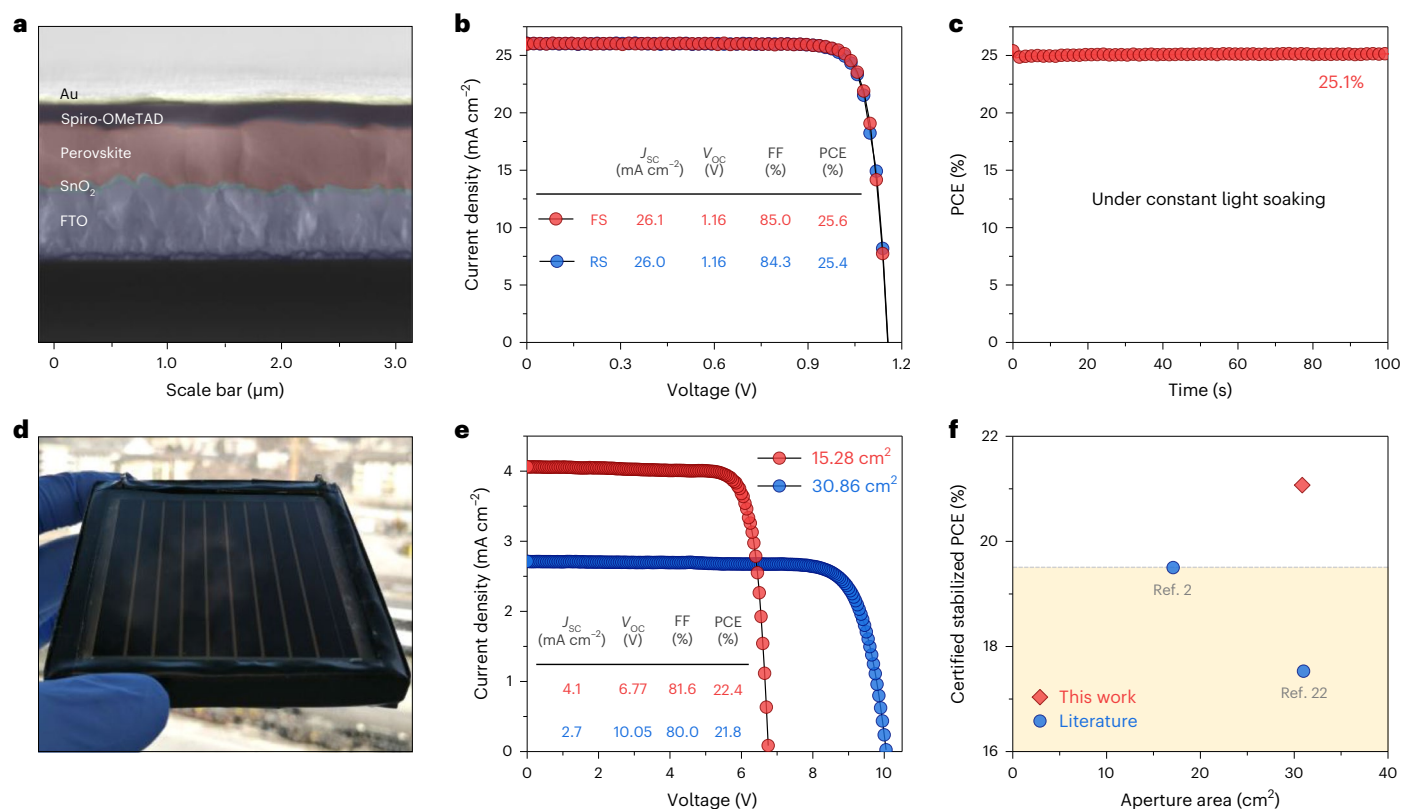
Fig. 3 | Photovoltaic performance of PSCs and perovskite solar modules.
a, Cross-sectional SEM image of the fabricated PSC. **b**, $J–V$ characteristics of
the best-performing device. FS, forward scan; RS, reverse scan. **c**, SPO of the
best device without encapsulation under AM 1.5G irradiation (Xe arc lamp,
100 mW cm^{-2}) at room temperature in nitrogen. **d**, Photograph of the nine-
subcell perovskite solar module with a size of 6.5 × 7 cm^2. **e**, $J–V$ characteristics
of two perovskite mini-modules with aperture area of 15.28 and 30.86 cm^2,
respectively. **f**, Statistics of certified stabilized PCEs as a function of device
area of n–i–p perovskite solar modules. The data points highlighted by a yellow
background indicate values previously reported in literature.

Au structure (Fig. 3a). The photovoltaic performance of these devices
was evaluated with control and TFPCBP-embedded perovskite films.
Control devices had PCEs of 23.5 ± 0.6%, while with TFPCBP the PCEs
were 25.1 ± 0.3% (Supplementary Fig. 18). The best TFPCBP device
showed a PCE of 25.6%, with negligible hysteresis (Fig. 3b) and a stabi-
lized power output (SPO) of 25.1% (Fig. 3c), compared with 24.4% for
the champion control device (Supplementary Fig. 19). The short-circuit
current density (J_{SC}) obtained from the current density–voltage ($J–V$)
characteristics was found to be consistent with the value integrated
from the external quantum efficiency (EQE) spectrum, with a relative
difference of less than 4% (Supplementary Fig. 20).

To investigate the impact of improved film homogeneity on
large-scale applications, we fabricated perovskite solar modules
using TFPCBP-embedded perovskite films (Fig. 3d). A module con-
sisting of six subcells with an aperture area of 15 cm^2 exhibited a high
PCE of 22.4% (corresponding to an active-area PCE of 24.1%) with an
open-circuit voltage (V_{OC}) of 6.77 V, a J_{SC} of 4.1 mA/cm^2 and a fill factor
(FF) of 81.6% (Fig. 3e). When the aperture area was doubled, the module
consisting of nine subcells with an aperture area of 31 cm^2 showed a
PCE of 21.8% (corresponding to an active-area PCE of 24.0%) with a
V_{OC} of 10.05 V, a J_{SC} of 2.7 mA/cm^2 and an FF of 80.0%. We sent the large
module to the National PV Industry Measurement and Testing Center
(NPVM) in China, a National Renewable Energy Laboratory-authorized
certification facility, for certification. The module achieved a PCE
of 21.6% (stabilized efficiency of 21.1%) with a V_{OC} of 10.03 V, a J_{SC} of
2.7 mA/cm^2 and an FF of 79.7% (Supplementary Fig. 21). These modules
possess, to the best of our knowledge, the highest certified PCE
value reported among n–i–p perovskite solar modules (Fig. 3f and
Supplementary Table 2)[2,22].

Stability study

To examine the stability of the perovskite films with and without
TFPCBP, we evaluated the degree of degradation when we subjected
the films to 85% relative humidity (RH) at 85 °C. The crystallographic
properties of the fresh and aged films were analysed and compared
(Supplementary Fig. 22). TFPCBP-embedded perovskite film exhib-
ited higher resistance to damp heat, as evidenced by the decreased
PbI$_2$-to-perovskite peak ratio (0.39) compared with that of the con-
trol film (0.85). Additionally, PL mapping revealed that the control
film suffered from a loss of photoactive phase after ageing, while the
TFPCBP-embedded perovskite film demonstrated a superior ability
to maintain its original phase under external stresses (Supplemen-
tary Fig. 23). Therefore, we posit that the TFPCBP-based devices had
improved stability.

To assess the impact of TFPCBP on device stability, we sub-
stituted the doped spiro-OMeTAD with poly[bis(4-phenyl)
(2,4,6-trimethylphenyl)amine] to eliminate this hole transport layer
(HTL) as a source of instability[23]. We tracked the performance of
unencapsulated solar cells under a ~45% RH ambient according to
ISOS-D-1 (ref. 24). Following 3,000 h of ageing, the cells showed a
low, 4% (relative) PCE loss for the TFPCBP-based device, compared
with 25% (relative) efficiency loss seen in the control devices (Fig.
4a). We then tested the solar cells under prolonged heat exposure
at 85 °C in nitrogen, applying the ISOS-D-2 procedure. TFPCBP-based
devices retained 94% of their initial PCE after 1,000 h of continu-
ous heating, while the control devices retained 78% of their initial
performance (Fig. 4b). Thermal cycling tests revealed similar
trends for control and TFPCBP devices when the temperature
was alternated between −40 °C and 85 °C (Supplementary Fig. 24).
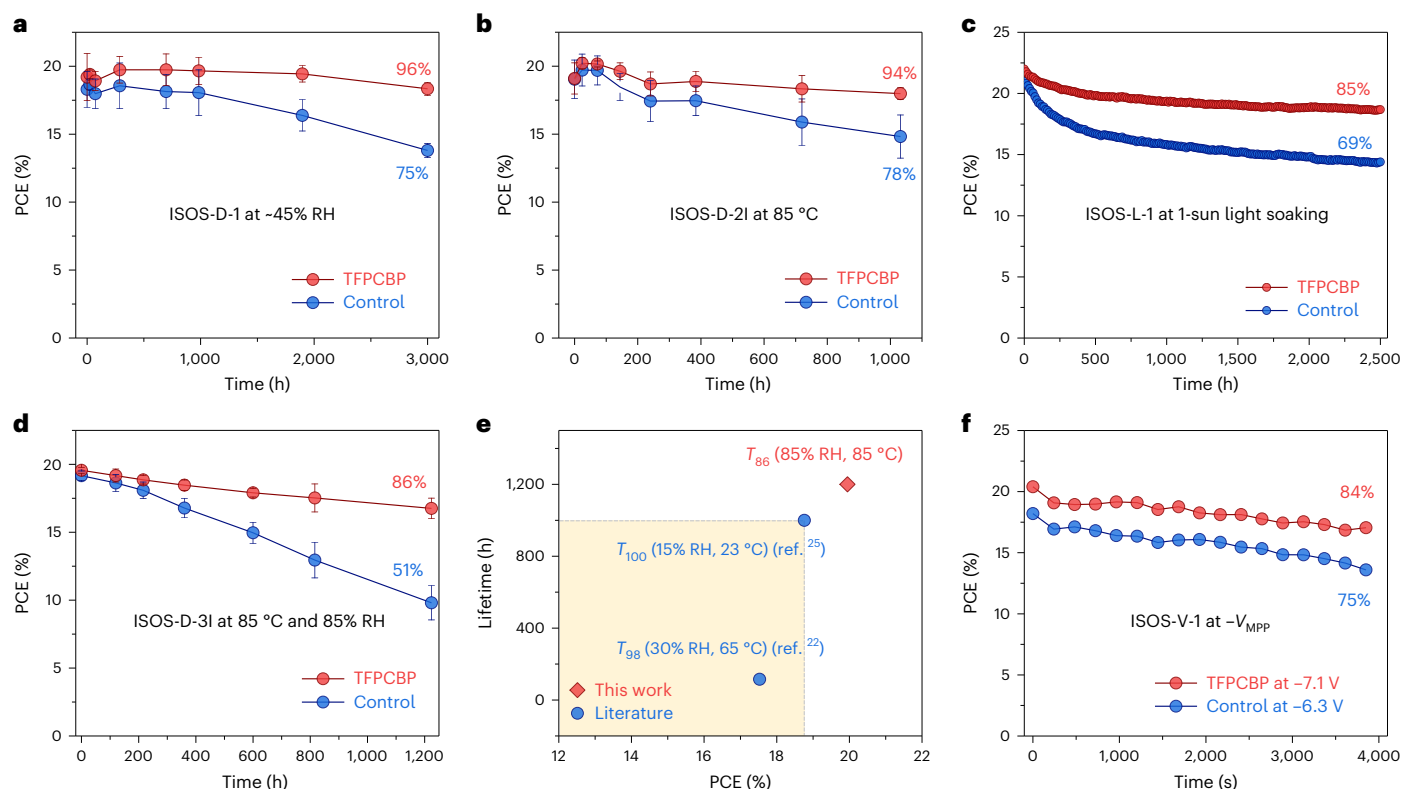
Fig. 4 | Stability of PSCs and perovskite solar modules. a. The humidity stability of unencapsulated small-sized PSCs in ambient air with ~45% RH at room temperature. Devices were periodically tested under AM 1.5G irradiation with a Xe arc lamp at 100 mW cm^{-2}. **b**, The thermal stability of unencapsulated small-sized PSCs under constant heating at 85 °C in N$_2$. Devices were periodically tested under AM 1.5G irradiation with a Xe arc lamp at 100 mW cm^{-2}. **c**, Continuous MPP tracking of the unencapsulated small-sized PSCs under 1-sun illumination with a white light-emitting diode (100 mW cm^{-2}) at 25 °C with a N$_2$ flow. **d**, The stability of the encapsulated perovskite modules stored in ambient air with ~85% RH and heating at 85 °C. Devices were periodically tested under AM 1.5G irradiation with

a Xe arc lamp at 100 mW cm^{-2}. **e**, Statistics of the combination of certified PCEs and damp-heat stability of n–i–p perovskite solar modules reported in literature. Data points highlighted by a yellow background indicate values previously reported in literature. **f**, The reverse bias stability of unencapsulated perovskite modules (eight subcells) biasing at the $-V_{MPP}$ in ambient air with ~30% RH in the dark at room temperature, simulating the condition with the bypass diode. Devices were periodically tested under AM 1.5G irradiation with a Xe arc lamp at 100 mW cm^{-2}. Data presented as mean ± s.d. in **a**, **b** and **d**, tracing the PCE of five devices over time for each condition.

The absence of thermotropic properties upon heating/cooling may be attributed to the fact that TFPCBP remains in a discrete molecular form in the final perovskite films, rather than crystalline: the larger molecular distance weakens intermolecular forces, and interactions between TFPCBP and perovskite may further diminish the impact of intermolecular forces on TFPCBP molecules. Operating stability was investigated under 1-sun illumination (ISOS-L-1). The TFPCBP device retained 85% of the initial PCE after maximum power point (MPP) operation over 2,500 h (Fig. 4c), compared with 69% PCE retention for the control device.

We then evaluated the damp-heat stability of encapsulated modules using the ISOS-D-3 procedure, subjecting them to 85% RH at 85 °C. The TFPCBP-based modules retained 86% of their initial efficiency after 1,200 h, compared with 51% retention for the control (Fig. 4d). This represents the longest-lived damp-heat stability in literature among n–i–p perovskite solar modules (Fig. 4e and Supplementary Table 2)[22,25]. In addition to damp-heat stability, the reverse bias stability is critical for solar modules as it mimics the scenario of partial shading of modules caused by clouds, dirt and trees, where shaded subcells are compelled to operate under reverse bias to match the current flow through the rest of the module[26,27]. To investigate this, we simulated both conditions without and with bypass diodes, that is, shading one of the subcells and applying a constant $-V_{MPP}$ (ISOS-V-1) in the dark. The shading tests were performed by entirely masking one of the subcells under 1-sun illumination.

As shown in Supplementary Fig. 25a, the target module exhibited a higher breakdown voltage of −11.68 V over −10.54 V for the control module and could recover 90% of its original efficiency compared with 80% for the control module after the shading test (Supplementary Fig. 25b). Figure 4f shows the performance of modules in the context of constant reverse bias stress. The target module subjected to a negative bias of $-V_{MPP}$ = −7.1 V exhibited superior reverse bias resilience, with 84% of the initial efficiency being retained over 1 h. In comparison, the control module retained 75% efficiency at $-V_{MPP}$ = −6.3 V.

Conclusion

In this study, we advanced a liquid crystal additive approach to realize a more homogeneous dispersion of additives and thus provide more uniform passivation of perovskite grains, leveraging the phase behaviour and functionalization properties offered by thermotropic liquid crystals. We found that TFPCBP led to the best results when comparing six liquid crystals, in terms of both film uniformity and photovoltaic performance. TFPCBP demonstrated a uniform distribution along the grain boundaries, which we linked to its high molecular diffusion during perovskite crystallization. The combined theoretical and experimental results indicate defect passivation from the electron-rich $-C_6H_2F_3$ group. This enabled perovskite modules with an aperture area of 31 cm^2 having a certified stabilized efficiency of 21.1% along with long-term environmental stability.

Methods

Materials

$SnCl_2 \cdot 2H_2O$ (99.99%), urea (99%), HCl acid (37 wt.% in water), thioglycolic acid (TGA, 98%), CsI (99.99%), 4-*tert*-butylpyridine (98%) and bis (trifluoromethanesulfonyl)-imide lithium salt (LiTFSI, 99.0%) were purchased from Sigma-Aldrich. PbI_2 (99.99%), FPCBP (98%), DFPCBP (98%), TFPCBP (98%), PTFPBH (98%), TFPTP (98%) and DMDFPBP (98%) were purchased from TCI America. Formamidinium iodide (FAI), methylammonium chloride (MACl), methylammonium iodide (MAI), phenylethylammonium iodide (PEAI) and FK209 Co(III) TFSI salt were purchased from Greatcell Solar Materials. All materials were used as received without purification. *N,N*-dimethylformamide (DMF, 99.8%), dimethyl sulfoxide (DMSO, 99.7%), isopropanol (99.8%), acetonitrile (99.9%) and chlorobenzene (99.8%) were purchased from Acros Organics. Spiro-OMeTAD and poly[bis(4-phenyl)(2,4,6-trimethylphenyl) amine] were from Xi'an Polymer Light Technology Corp.

Solar cell fabrication

An electron transport layer (ETL) was deposited on precleaned FTO substrates by the chemical bath deposition (CBD) method. The CBD solution was prepared by mixing 1.25 g urea, 1.25 ml HCl, 25 μl TGA and 275 mg $SnCl_2 \cdot 2H_2O$ in 100 ml deionized water. The substrates were put into a staining dish immersed in the above solution in an oven at 90 °C for 5 h. After cooling down to room temperature, the substrates were taken out for washing with isopropanol and then annealing at 190 °C for 1 h. Before perovskite deposition, the FTO/SnO_2 substrates were treated with ultraviolet ozone. The perovskite solution was prepared by adding 1.60 M PbI_2, 1.37 M FAI, 0.52 M MACl, 0.08 M MAI and 0.07 M CsI to mixed DMF and DMSO solution with a volume ratio of 4:1. Liquid crystals (4 mol%) were added to the perovskite precursor relative to PbI_2. The perovskite films were deposited at 1,000 r.p.m. for 10 s and 5,000 r.p.m. for 30 s, respectively, at room temperature. At 20 s during the second step, 150 μl chlorobenzene was dropped on the spinning films to facilitate perovskite nucleation and crystallization. The films were then annealed at 100 °C for 50 min and 150 °C for 10 min. Then, 20 mM PEAI solution in isopropanol was spin-coated on the perovskite films at 5,000 r.p.m. for 20 s at room temperature. For the HTL, 0.06 M spiro-OMeTAD was dissolved in chlorobenzene with additives of 0.2 M 4-*tert*-butylpyridine, 0.03 M LiTFSI in acetonitrile, and 0.0035 M FK209 Co(III) TFSI salt in acetonitrile. The spiro-OMeTAD layer was deposited by spin-coating at 3,000 r.p.m. for 20 s at room temperature. Finally, 70 nm gold electrodes were thermally evaporated under a vacuum of 10^{-7} torr. The substrates were maintained at 20 °C during the deposition.

Module fabrication

Perovskite solar modules consisted of six and eight subcells connected in series on 6.5 cm × 7 cm and 5 cm × 5 cm substrates, respectively. FTO substrates were laser-scribed using a 1,064 nm nanosecond Yb-fibre laser with a power of 20 W and a frequency of 65 kHz (Trotec). P1 lines (50 μm wide) were used to separate subcells. The deposition processes for the ETL, passivation layer and HTL were the same as for the solar cells. The perovskite films were deposited by vacuum-flash solution processing in a N_2-filled glovebox. The perovskite precursor (1.3 M) was spin-coated at 1,000 r.p.m. for 10 s and 5,000 r.p.m. for 20 s, respectively. The substrates were immediately transferred into a vacuum chamber and quickly pumped to a vacuum level of 2–5 Pa at 100 °C. After 20 s, the chamber was vented, and the perovskite films were annealed at 100 °C for 50 min and 150 °C for 10 min. Then 150-μm-wide P2 lines were patterned by a 1,030 nm picosecond CO_2 laser with a power of 0.4 W and a frequency of 200 kHz (LPKF ProtoLaser R). After the gold deposition, 100-μm-wide P3 lines were laser-scribed to complete the module fabrication. The same laser, power and frequency were used for P2 and P3. The geometric fill factor was 93% and 91% for the small (15 cm²) and large (31 cm²) modules, respectively.

Characterizations

The *J–V* characteristics were measured in air at room temperature using a Keithley 2400 source under simulated air mass 1.5 global (AM 1.5G) irradiation (100 mW cm⁻²) using a Xe arc lamp from a Sciencetech A1 Light Line Class AAA solar simulator (calibrated by a reference solar cell from Sciencetech (SCI-REF-Q) before measurement). No preconditioning of the device was applied before the measurement. The scanning step was 20 mV for solar cells and 50 mV for modules. The scanning rate was 70 mV s⁻¹. The active area of the solar cells was defined by an opaque metal mask with a square aperture of area of 0.0625 cm². The aperture area of small and large modules was defined by an opaque metal mask with rectangular apertures of 15.28 and 30.86 cm², respectively.

Operational stability tests were performed on the unencapsulated solar cells with a nitrogen flow of ~30 ml min⁻¹ under 1-sun illumination from a white light-emitting diode. For humidity stability testing, the unsealed solar cells were kept in ambient with ~45% RH monitored by a hygrometer at room temperature in the dark. For thermal stability testing, the unencapsulated solar cells were heated at 85 °C in nitrogen in the dark. The damp-heat stability test was conducted on the encapsulated modules in a sealed box with ~85% RH and an 85 °C atmosphere. The reverse bias stability testing with bypass diodes was conducted by applying a constant $-V_{MPP}$ on the perovskite module in the dark. Thermal cycling stability measurements were conducted between 233 and 358 K using a heating and cooling stage with a ramp rate of 20 °C per minute in the dark.

EQE spectra were taken using an Enlitech QE-R spectrometer. ToF-SIMS measurements were conducted on an IONTOF M6 instrument with a primary Bi source of 30 keV and an analysis area of 50 × 50 μm². SEM images were taken by using a JEOL JSM-7900FLV. The operating voltages for surface and cross-section images were 5 kV and 15 kV, respectively. PL mapping was conducted on a Nano Raman and TERS system integrated with SWIFT and DuoScan technologies. A 473 nm laser was used for excitation. KPFM was performed on a Bruker photocurrent and thermal atomic force microscope with Pt/Ir-coated cantilevers. The scan rate was 0.25 Hz, and the scan area was 5 × 5 μm². The PLQY of the solid films was collected by a fibre-coupled spectrometer (QE-Pro Ocean Optics) in an integrating sphere under excitation by a power-tunable continuous wave diode laser (405 nm). The power of the excitation light was measured in free space by a power meter (Ophir). FTIR spectroscopy was performed on a Bruker Tensor 37. Time-resolved photoluminescence (TRPL) spectra were collected using an FS5 spectrofluorometer (Edinburgh Instruments) with an excitation wavelength of 373 nm. XPS was performed on the NEXSA G2 instrument with an X-ray spot size of 200 μm. Samples were etched by Ar ion sputtering for 10 s before the measurement. XRD patterns were collected using a Rigaku Miniflex diffractometer with Cu $K\alpha_1$ radiation. GIWAXS measurements were conducted at the Brockhouse X-ray Diffraction and Scattering Sector Low Energy Wiggler beamline of the Canadian Light Source[28]. An energy of 15.12 keV ($\lambda = 0.82$ Å) was selected using a Si(111) monochromator. Patterns were collected on a Rayonix MX300 detector operating in 8 × 8 binning mode, placed at a distance of 328.04 mm from the sample. A 4.0 mm circular beamstop with an embedded photodiode was used to block the direct beam and to align the sample height and incident angle (theta). Images were calibrated using LaB6 (NIST SRM 660b) and processed via the Nika software package[29] and the GIXSGUI MATLAB plug-in[30]. High spatial resolution structural and chemical characterizations were conducted on an JEOL ARM 200CF operated at 200 keV and equipped with a probe corrector and dual solid silicon drift detectors. The electron transparent samples were drop-cast on a lacey carbon grid. The contact angle was measured on a VCA Optima XE.

DFT calculations

First-principles calculations based on DFT were carried out using the Vienna Ab initio Simulation Package[31]. The generalized

gradient approximation of the Perdew–Burke–Ernzerhof functional was employed as the exchange–correlation functional[32]. The DFT-D3 method for the van der Waals correction was included[33]. The plane-wave cut-off energy was 400 eV. The energy and force convergence criteria were set to 10^{-5} eV and 0.03 eV Å^{-1}, respectively. The binding energies (E_b) of ligands with the perovskite surface were calculated as E(ligand@perovskite) − E(ligand) − E(perovskite), where E(structure) is the total energy of the corresponding structures. The electrostatic potentials of the ligands were calculated in the Gaussian 09 package at the B3LYP/def2TZVP level with DFT-D3.

Reporting summary

Further information on research design is available in the Nature Portfolio Reporting Summary linked to this article.

Data availability

All data generated or analysed during this study are included in the published article and its Supplementary Information and Source Data files. Source data are provided with this paper.

References

1. Ding, Y. et al. Single-crystalline TiO₂ nanoparticles for stable and efficient perovskite modules. *Nat. Nanotechnol.* **17**, 598–605 (2022).
2. You, S. et al. Radical polymeric p-doping and grain modulation for stable, efficient perovskite solar modules. *Science* **379**, 288–294 (2023).
3. Liu, C. et al. Tuning structural isomers of phenylenediammonium to afford efficient and stable perovskite solar cells and modules. *Nat. Commun.* **12**, 6394 (2021).
4. Park, J. et al. Controlled growth of perovskite layers with volatile alkylammonium chlorides. *Nature* **616**, 724–730 (2023).
5. Bu, T. et al. Lead halide-templated crystallization of methylamine-free perovskite for efficient photovoltaic modules. *Science* **372**, 1327–1332 (2021).
6. Green, M. A. et al. Solar cell efficiency tables (version 60). *Prog. Photovolt. Res. Appl.* **30**, 687–701 (2022).
7. Yang, M. et al. Perovskite ink with wide processing window for scalable high-efficiency solar cells. *Nat. Energy* **2**, 17038 (2017).
8. Ren, A. et al. Efficient perovskite solar modules with minimized nonradiative recombination and local carrier transport losses. *Joule* **4**, 1263–1277 (2020).
9. Jiang, Q. et al. Surface passivation of perovskite film for efficient solar cells. *Nat. Photonics* **13**, 460–466 (2019).
10. Yang, Y. et al. Bi-functional additive engineering for high-performance perovskite solar cells with reduced trap density. *J. Mater. Chem. A* **7**, 6450–6458 (2019).
11. Zhang, Y. et al. A strategy to produce high efficiency, high stability perovskite solar cells using functionalized ionic liquid-dopants. *Adv. Mater.* **29**, 1702157 (2017).
12. Jeong, J. et al. Pseudo-halide anion engineering for α-FAPbI₃ perovskite solar cells. *Nature* **592**, 381–385 (2021).
13. Min, H. et al. Hot-casting-assisted liquid additive engineering for efficient and stable solar cells. *Adv. Mater.* **34**, 2205309 (2022).
14. Li, N. et al. Cation and anion immobilization through chemical bonding enhancement with fluorides for stable halide perovskite solar cells. *Nat. Energy* **4**, 408–415 (2019).
15. Bai, S. et al. Planar perovskite solar cells with long-term stability using ionic liquid additives. *Nature* **571**, 245–250 (2019).
16. Liu, Y., Lorenz, M., Ievlev, A. V. & Ovchinnikova, O. S. Secondary Ion Mass Spectrometry (SIMS) for chemical characterization of metal halide perovskites. *Adv. Funct. Mater.* **30**, 2002201 (2020).
17. Kim, D. H., Whitaker, J. B., Li, Z., van Hest, M. F. A. M. & Zhu, K. Outlook and challenges of perovskite solar cells toward terawatt-scale photovoltaic module technology. *Joule* **2**, 1437–1451 (2018).
18. Li, M.-H. et al. Highly efficient 2D/3D hybrid perovskite solar cells via low-pressure vapor-assisted solution process. *Adv. Mater.* **30**, 1801401 (2018).
19. Mihály, J. et al. FTIR and FT-raman spectroscopic study on polymer based high pressure digestion vessels. *Croat. Chem. Acta* **79**, 497–501 (2006).
20. Brakkee, R. & Williams, R. M. Minimizing defect states in lead halide perovskite solar cell materials. *Appl. Sci.* **10**, 3061 (2020).
21. Wang, R. et al. Constructive molecular configurations for surface-defect passivation of perovskite photovoltaics. *Science* **366**, 1509–1513 (2019).
22. Yoo, J. W. et al. Efficient perovskite solar mini-modules fabricated via bar-coating using 2-methoxyethanol-based formamidinium lead tri-iodide precursor solution. *Joule* **5**, 2420–2436 (2021).
23. Zhao, Y. et al. Inactive (PbI₂)₂RbCl stabilizes perovskite films for efficient solar cells. *Science* **377**, 531–534 (2022).
24. Khenkin, M. V. et al. Consensus statement for stability assessment and reporting for perovskite photovoltaics based on ISOS procedures. *Nat. Energy* **5**, 35–49 (2020).
25. Zhu, J. et al. Formamidine disulfide oxidant as a localised electron scavenger for >20% perovskite solar cell modules. *Energy Environ. Sci.* **14**, 4903–4914 (2021).
26. Wang, C. et al. Perovskite solar cells in the shadow: understanding the mechanism of reverse-bias behavior toward suppressed reverse-bias breakdown and reverse-bias induced degradation. *Adv. Energy Mater.* **13**, 2203596 (2023).
27. Bowring, A. R., Bertoluzzi, L., O'Regan, B. C. & McGehee, M. D. Reverse bias behavior of halide perovskite solar cells. *Adv. Energy Mater.* **8**, 1702365 (2018).
28. Leontowich, A. F. G. et al. The lower energy diffraction and scattering side-bounce beamline for materials science at the Canadian Light Source. *J. Synchrotron Radiat.* **28**, 961–969 (2021).
29. Ilavsky, J. Nika: software for two-dimensional data reduction. *J. Appl. Crystallogr.* **45**, 324–328 (2012).
30. Jiang, Z. GIXSGUI: a MATLAB toolbox for grazing-incidence X-ray scattering data visualization and reduction, and indexing of buried three-dimensional periodic nanostructured films. *J. Appl. Crystallogr.* **48**, 917–926 (2015).
31. Kresse, G. & Furthmüller, J. Efficient iterative schemes for ab initio total-energy calculations using a plane-wave basis set. *Phys. Rev. B* **54**, 11169–11186 (1996).
32. Perdew, J. P., Burke, K. & Ernzerhof, M. Generalized gradient approximation made simple. *Phys. Rev. Lett.* **77**, 3865–3868 (1996).
33. Lee, K., Murray, É. D., Kong, L., Lundqvist, B. I. & Langreth, D. C. Higher-accuracy van der Waals density functional. *Phys. Rev. B* **82**, 081101 (2010).

Author contributions

B.C., M.K.N., M.G.K. and E.H.S. supervised the project. Y.Y. conceived the idea. Y.Y. and C.L. designed the experiments and performed the main characterizations. J.X. designed and conducted the DFT calculations. Y.D. and B.D. helped to perform solar cell and module fabrication. J.Y. and X.H. conducted the TEM measurements. J.L. helped with the crystallography analysis. S.S.H., V.K.S. and M.C.H. conducted the thermal cycling stability test. L.G. performed the PLQY and GIWAXS measurements and was helpful with the data analysis. A.S.R.B. conducted the contact angle test. A.L., H.Z. and S.M.P. were helpful with the construction of the paper and revised the paper. Y.Y. wrote the first draft of the paper. All the authors revised and approved the paper.

Competing interests

The authors declare no competing interests.

Additional information

natureresearch

Corresponding author(s): Bin Chen, Mohammad K. Nazeeruddin, Mercouri G. Kanatzidis, Edward H. Sargent

Solar Cells Reporting Summary

Nature Research wishes to improve the reproducibility of the work that we publish. This form is intended for publication with all accepted papers reporting the characterization of photovoltaic devices and provides structure for consistency and transparency in reporting. Some list items might not apply to an individual manuscript, but all fields must be completed for clarity.

For further information on Nature Research policies, including our data availability policy, see Authors & Referees.

▶ Experimental design

Please check: are the following details reported in the manuscript?

1. Dimensions

Area of the tested solar cells	☒ Yes ☐ No	The aperture area for the solar cells was 0.0625 cm2 (Methods). The aperture area for small and large modules was 15.28 cm2 and 30.86 cm2, respectively (Method-Characterization).
Method used to determine the device area	☒ Yes ☐ No	The aperture area of the solar cells was defined by an opaque metal mask with square aperture of area of 0.0625 cm2 (Methods). The aperture area of small and large modules was defined by an opaque metal mask with rectangular apertures of 15.28 and 30.86 cm2, respectively (Method-Characterization).

2. Current-voltage characterization

Current density-voltage (J-V) plots in both forward and backward direction	☒ Yes ☐ No	See Figure 3b and Supplementary Fig. 19.
Voltage scan conditions *For instance: scan direction, speed, dwell times*	☒ Yes ☐ No	The scanning step was 20 mV for solar cells and 50 mV for modules. The scanning rate was 70 mV/s (Method-Characterization).
Test environment *For instance: characterization temperature, in air or in glove box*	☒ Yes ☐ No	Current density (J)-voltage (V) characteristics of the unencapsulated devices were characterized at room temperature in air (Method-Characterization).
Protocol for preconditioning of the device before its characterization	☒ Yes ☐ No	No preconditioning of the device was applied before the measurement (Method-Characterization).
Stability of the J-V characteristic *Verified with time evolution of the maximum power point or with the photocurrent at maximum power point; see ref. 7 for details.*	☒ Yes ☐ No	See Figure 4c and Main Text Page 9.

3. Hysteresis or any other unusual behaviour

Description of the unusual behaviour observed during the characterization	☒ Yes ☐ No	The devices showed negligible hysteresis behaviors (Main Text Page 6).
Related experimental data	☒ Yes ☐ No	See Figure 3b and Supplementary Fig. 19.

4. Efficiency

External quantum efficiency (EQE) or incident photons to current efficiency (IPCE)	☒ Yes ☐ No	See Supplementary Fig. 20.
A comparison between the integrated response under the standard reference spectrum and the response measure under the simulator	☒ Yes ☐ No	The JSC obtained from the J-V characteristics was found to be consistent with the value integrated from the external quantum efficiency (EQE) spectrum, with a relative difference of less than 4%. (Supplementary Fig. 20).
For tandem solar cells, the bias illumination and bias voltage used for each subcell	☐ Yes ☒ No	No tandem solar cell was reported in this manuscript.

5. Calibration

Light source and reference cell or sensor used for the characterization	☒ Yes ☐ No	Light source is a Xe arc lamp from a ScienceTech A1 Light Line Class AAA solar simulator. The reference solar cell is from Sciencetech (SCI-REF-Q) (Method-Characterization).

Confirmation that the reference cell was calibrated and certified	☒ Yes ☐ No	The light intensity was calibrated by the reference solar cell (SCI-REF-Q) from Sciencetech (Method-Characterization).
Calculation of spectral mismatch between the reference cell and the devices under test	☐ Yes ☒ No	We rely on certified efficiency results.

6. Mask/aperture

Size of the mask/aperture used during testing	☒ Yes ☐ No	The active area of the solar cells was defined by an opaque metal mask with square aperture of the area of 0.0625 cm2 (Methods). The aperture area of small and large modules was defined by an opaque metal mask with rectangular apertures of 15.28 and 30.86 cm2, respectively (Methods).
Variation of the measured short-circuit current density with the mask/aperture area	☐ Yes ☒ No	We didn't measure the solar cells with apertures of different sizes.

7. Performance certification

Identity of the independent certification laboratory that confirmed the photovoltaic performance	☒ Yes ☐ No	National PV Industry Measurement and Testing Center (NPVM) in China
A copy of any certificate(s) *Provide in Supplementary Information*	☒ Yes ☐ No	Supplementary Fig. 21

8. Statistics

Number of solar cells tested	☒ Yes ☐ No	20 devices for each condition were tested (Supplementary Fig. 18).
Statistical analysis of the device performance	☒ Yes ☐ No	Supplementary Fig. 18 and Main Text Page 6

9. Long-term stability analysis

Type of analysis, bias conditions and environmental conditions *For instance: illumination type, temperature, atmosphere humidity, encapsulation method, preconditioning temperature*	☒ Yes ☐ No	Operational stability tests were performed on the unencapsulated solar cells with a nitrogen flow of ~30 mL/min under 1-sun illumination from a white LED. For the humidity stability, the unsealed solar cells were kept in the ambient of ~45% relative humidity (RH) monitored by a hygrometer at room temperature in the dark. For the thermal stability, the unencapsulated solar cells were heated at 85℃ in nitrogen in the dark. The damp-heat stability test was conducted on the encapsulated modules in a sealed box with ~85% RH and 85˚C atmosphere. The reverse bias stability with bypass diodes was conducted by applying a constant -Vmpp on the perovskite module in the dark. (See Fig. 4 and Method-Characterization)